ACS OMEGA

http://pubs.acs.org/journal/acsodf

Article

High Uniformity and Enhancement Au@AgNS 3D Substrates for the Diagnosis of Breast Cancer

Zhengxia Yang, Hai-Sheng Su,* En-Ming You, Siying Liu, Zihang Li, and Yun Zhang*

Cite This: *ACS Omega* 2022, 7, 15223−15230

Read Online

ACCESS | Metrics & More | Article Recommendations | Supporting Information

ABSTRACT: Breast cancer appears to be one of the leading causes of cancer-related morbidity and mortality for women worldwide. The accurate and rapid diagnosis of breast cancer is hence critical for the treatment and prognosis of patients. With the vibrational fingerprint information and high detection sensitivity, surface-enhanced Raman spectroscopy (SERS) has been extensively applied in biomedicine. Here, an optimized bimetallic nanosphere (Au@Ag NS) 3D substrate was fabricated for the aim of the diagnosis of breast cancer based on the SERS analysis of the extracellular metabolites. The unique stacking mode of 3D Au@Ag NSs provided multiple plasmonic hot spots according to the theoretical calculations of the electromagnetic field distribution. The low relative standard deviation (RSD = 2.7%) and high enhancement factor (EF = 1.42×10^5) proved the uniformity and high sensitivity. More importantly, the normal breast cells and breast cancer cells could be readily distinguished from the corresponding SERS spectra based on the extracellular metabolites. Furthermore, the clear clusters of SERS spectra from MCF-7 and MDA-MB-231 extracellular metabolites in the orthogonal partial least-squares discriminant analysis plot indicate the distinct metabolic fingerprint between breast cancer cells, which imply their potential clinical application in the diagnosis of breast cancer.

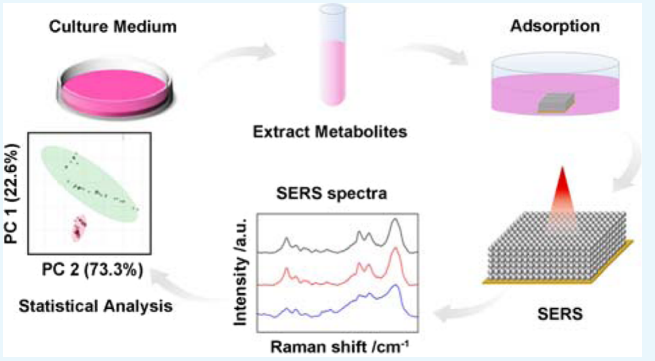

1. INTRODUCTION

Breast cancer remains an invisible killer for women around the world, and its risk increases with aging.[1,2] The diagnosis and treatment have significantly improved the survival rates and tremendously reduced the probability of transforming into malignant tumors. Therefore, the accurate diagnosis of breast cancer is the most crucial step for the prognosis of patients.[3] The biopsy is currently the gold standard for breast cancer diagnosis and provides accurate tumor histological information.[4,5] However, sample extraction is time-consuming, which brings much pain and risk to patients.[6,7] The imaging information of breast cancer can be obtained by magnetic resonance imaging (MRI), which can sensitively identify multiple centers and lesions.[8,9] Nevertheless, it is difficult for MRI to distinguish the states of tumors when the benign tumors transform into malignant ones. Thus, further confirmation is required which delays the optimal period for the treatment.[10,11] The most effective and economical method for breast cancer screening is mammography, but the sensitivity is often limited.[12] Therefore, there is a pressing need to develop noninvasive, rapid, and highly sensitive diagnosis methods for breast cancer.

Screening of breast cancer biomarkers from metabolites is a promising method toward this direction. The cell metabolites which are closely related to the phenotype and the functional execution of the organism play a key role in the cell function.[13,14] In recent years, the markers screened from metabolites via noninvasive ways have shown great prospects in the diagnosis of breast cancer.[14] However, it remains challenging to detect the cell metabolites with the trace amount. To this end, surface-enhanced Raman spectroscopy (SERS) seems to be a potent technique. With the Raman fingerprint information, the ultrahigh sensitivity down to the single molecule has been achieved by SERS, which makes it a powerful tool in the analysis of biomolecules.[15−17] SERS has also been widely explored for the diagnosis and treatment of cancers, such as nasopharyngeal, pancreatic, prostate, and oral cancer.[18−22] For the practical application, the SERS sensitivity is determined by the SERS substrate. Therefore, the fabrication of substrates with high SERS enhancement is pivotal.[23,24] In addition, the SERS signal from the gaps between the nanostructure (which term as hot spots) contributes to the majority of the overall SERS intensity.[23] Consequently, the 3D substrates seem to be an appealing platform.[25−27] Notably, in

Received: March 10, 2022
Accepted: April 8, 2022
Published: April 24, 2022

addition to the intralayer gaps within the nanostructure layers, there are extra interlayer gaps between the different layers in the 3D SERS substrate, leading to the effective adsorption and enrichment of target molecules.[25,26] Furthermore, noble metals such as Au and Ag are the most active SERS materials.[28] Ag exhibits superior SERS performance, while Au has advantages in terms of chemical stability.[29] The merits of Au and Ag can be combined in the bimetallic nanospheres (Au@Ag NSs) with novel optical properties.[29] Consequently, the Au@Ag NSs were selected as the building block to fabricate the 3D substrate in this study.

Herein, we reported an Au@Ag NS 3D SERS substrate with high uniformity and sensitivity for the analysis of metabolites toward the diagnosis of breast cancer. The optimized Au@Ag NS 3D SERS substrate realized the quantitative detection of melamine with a low detection limit (LOD) of 82 nM. Moreover, the Au@Ag NS 3D substrate was used to analyze the extracellular metabolites of normal breast cells (MCF-10A) and breast cancer cells (MCF-7 and MDA-MB-231). The statistical analysis methods were further used to help differentiate MCF-10A, MCF-7, and MDA-MB-231 extracellular metabolites based on the SERS spectra. Particularly, the breast cancer cells were clearly distinct from the normal breast cell and different breast cancer cells could also be identified. In addition, the SERS-based detection of extracellular metabolites of breast cancer cells has potential to determine the biomarkers of different breast cancer. These results provide new methods for the clinical diagnosis of breast cancer.

2. EXPERIMENTAL SECTION

2.1. Reagents. Hexadecyl trimethyl ammonium bromide (CTAB, 99%), gold chloride trihydrate ($HAuCl_4{\cdot}3H_2O$, 99%), 4-mercaptobenzoic acid (4-MBA, 99%), sodium borohydride ($NaBH_4$, 99%), poly(vinylpyrrolidone) (PVP ≈ 55,000), and hexadecyl trimethyl ammonium chloride (CTAC, 99%) were purchased from Sigma-Aldrich. Ascorbic acid (AA, 99.99%), ethanol (99%), and silver nitrate ($AgNO_3$, 99%) were purchased from Xilong Scientific. Melamine was obtained from Shanghai Aladdin Biochemical Technology Co., Ltd. Cyclohexane (99%), dichloromethane (99%), octane (99%), and methanol were purchased from Sinopharm Group Chemical Reagent Co., Ltd., Shanghai. The experimental solutions were prepared with ultra-pure Milli-Q water (18.2 MΩ) or ethanol. The glassware was soaked in freshly prepared aqua regia and then rinsed with plenty of ultra-pure Milli-Q water.

2.2. Preparation of AuNSs. AuNSs were synthesized following the guidance of the previous reports with some modifications.[30] First, 0.25 mL of 0.01 M $HAuCl_4{\cdot}3H_2O$ aqueous solution and 9.75 mL of 0.1 M CTAB solution were mixed. Then 0.60 mL of 0.01 M fresh ice-cold $NaBH_4$ solution was quickly injected under vigorous stirring. The mixture was gently stirred for 3 h at 28 °C to obtain seed solution. For the growth of AuNSs, 0.12 mL of the seed solution was added into 190 mL of H_2O containing 9.75 mL of 0.1 M CTAB followed by the addition of 4 mL of 0.01 M $HAuCl_4{\cdot}3H_2O$ and 15 mL of 0.1 M ascorbic acid. The growth solution was left undisturbed in water bath at 28 °C overnight. The final solution was centrifuged at 10,000 rpm for 10 min and redispersed in ultrapure water for the further use. In this step, AuNSs with a diameter of 27.6 ± 1.0 nm are obtained. To obtain AuNSs with a larger diameter, the AuNSs (27.6 ± 1.0 nm) prepared in the previous step were used as seeds. 1 mL of as-prepared AuNSs, 0.75 mL of 0.1 M AA, and 1.5 mL of 0.01 M $HAuCl_4{\cdot}3H_2O$ were injected into 30 mL of 0.025 M CTAC sequentially. The mixed solution was then placed in a water bath at 45 °C for 3 h. The formed Au nanoparticles was centrifuged at 5000 rpm for 10 min and redispersed in 30 mL of 0.02 M CTAB. Finally, 0.2 mL of 0.01 M $HAuCl_4{\cdot}3H_2O$ was added. The prepared solution was placed in water bath at 45 °C for 2 h. The formed AuNSs were centrifuged and redispersed in ultrapure water.

2.3. Preparation of Au@Ag NSs. In order to acquire Au@Ag NSs, 1 mL of the as-prepared AuNSs was added into 9 mL of ultrapure water. Then, 10 mL of 80 mM CTAC solution was injected. After stabilizing for a few minutes in water bath at 60 °C, 120 μL of 10 mM $AgNO_3$ and 150 μL of 0.1 M AA were added dropwise. The reaction solution was left undisturbed at 60 °C for 3 h, then centrifuged, and redispersed in ultrapure water. The thickness of silver shell can be regulated by controlling the amount of $AgNO_3$ and AA.

2.4. Gas−Liquid Interface-Mediated Au@Ag NSs Self-Assembly. 1% PVP ethanol solution was added to the Au@Ag NSs solution. After ultrasonication for 3 h, the mixture was centrifuged and redispersed in ethanol. Then 200 μL of dichloromethane, 200 μL of cyclohexane, and 30 μL of octane were added into 200 μL of Au@Ag NSs and mixed gently. The mixture was dropped on the water surface. Soon after, a single layer of Au@Ag NSs formed. After the evaporation of organic solvent, the Au@Ag NSs monolayer was transferred onto the silicon wafer. By repeating this procedure, different layers of Au@Ag NS substrates were fabricated to generate 3D structures.

2.5. SERS Intensity Comparison of Monolayer AuNS and Au@Ag NS Substrate. AuNSs and Au@Ag NSs were assembled on silicon wafer through the gas−liquid interface-mediated self-assembly in the form of a single layer. Prepared substrates were immersed in 1 mL of 0.1 mM solution of 4-MBA for 2 h. Then substrates were washed 3 times and dried at room temperature. The Raman signals were recorded with LabRAM Aramis Confocal Raman Microscopy (Horiba Jobin Yvon S.A.S.) with a 10 × (NA = 0.25) objective and 1s exposure time. To guarantee the accuracy, SERS mapping was performed with an area of 25 × 25 μm^2. The laser power was 1.76 mW.

2.6. Characterization of Nanoparticles and Substrates. The SERS activities were examined with the excitation wavelengths of 633 nm using 4-MBA as the probe. Au@Ag NS substrates were immersed in 1 mM 0.1 mM 4-MBA ethanol solutions for 2 h at room temperature. The substrates were then washed with ethanol and dried at room temperature. The Raman signal was recorded with LabRAM Aramis Confocal Raman Microscopy (Horiba Jobin Yvon S.A.S.) with a 10 × (NA = 0.25) objective and 1s exposure time. To guarantee the accuracy, SERS mapping was performed with an area of 25 × 25 μm^2. The laser power was 1.76 mW. Transmission electron microscopy (TEM) images, scanning electron microscopy (SEM) images, extinction spectra, and scanning TEM-energy dispersive X-ray spectroscopy element mapping were obtained by the HITACH H-7650 microscope, HITACH S-4800, and Agilent 5000 UV/Vis/NIR spectrophotometer, and Tecnai F30 (FEI, U.S.A), respectively.

2.7. Quantitative Analysis of Melamine. The Au@Ag NS 3D substrates were immersed in 1 mL aqueous solution of melamine with different concentrations (10^{-2} M to 10^{-7} M)

https://doi.org/10.1021/acsomega.2c01453
ACS Omega 2022, 7, 15223−15230

Scheme 1. Scheme of the Synthesis of Nanoparticles, Assembly of Au@Ag NS Substrate, Detection of Extracellular Metabolites, and Statistical Analysis of SERS Spectra

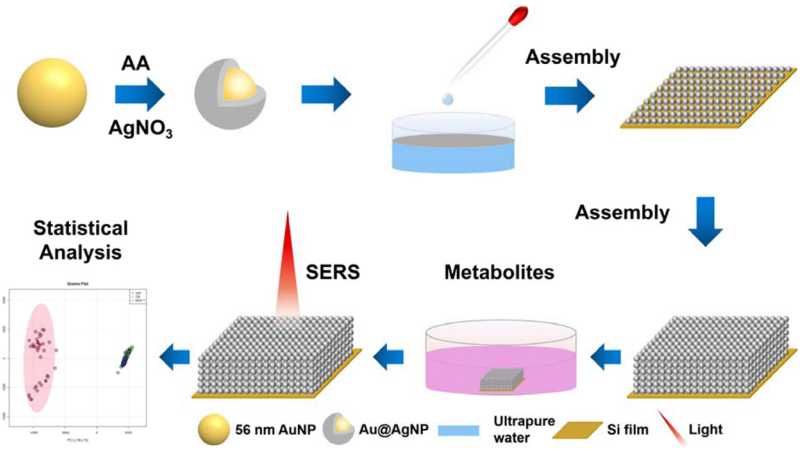

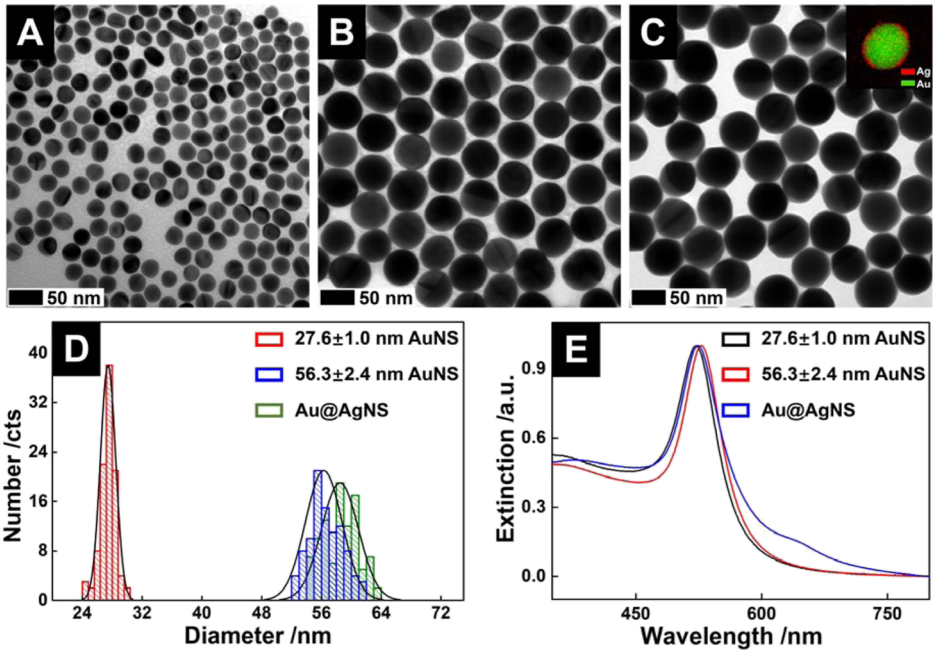

Figure 1. (A–C) TEM images of 27.6 ± 1.0 nm AuNSs, 56.3 ± 2.4 nm AuNSs, and 58.7 ± 2.7 nm Au@Ag NSs, respectively. The scale bar is 50 nm for TEM images. The inset in (C) presents the EDS elemental mapping of Au@Ag NSs. (D) Distribution of diameter of 27.6 ± 1.0 nm AuNSs, 56.3 ± 2.4 nm AuNSs, and 58.7 ± 2.7 nm Au@Ag NSs. (E) UV–vis–NIR absorption spectra.

for 2 h. Then, the substrate was washed three times and dried at room temperature. The experimental conditions are consistent with the detection of 4-MBA.

2.8. Analysis of Cell Metabolites. Cell culture media of three cell strains (MCF-10, MCF-7, and MDA-MB-231) were collected. To remove proteins and quench enzymatic reactions, 4 mL of media was mixed with 8 mL of methanol and then stored at −20 °C for 1 h. Subsequently, the mixture was centrifuged at 13,000 rpm for 30 min at 4 °C. Supernatants were lyophilized and resuspended in deionized water at the same concentration. Then, the samples were dissolved in water with the concentration of 0.07 g/mL for the following treatment of SERS substrate. Afterward, the optimal Au@Ag NS 3D substrates were immersed in the samples for 2 h. The substrates were washed and dried at room temperature. The Raman signal was recorded with LabRAM Aramis Confocal Raman Microscopy (Horiba Jobin Yvon S.A.S.) with a 10 × (NA = 0.25) objective and 1 s exposure time. For accuracy, SERS mapping was performed with an area of 25 × 25 μm^2. The laser power was 1.76 mW.

2.9. Data Processing. Baseline correction was processed with NGSLabSpec software. To identify changes of extracellular metabolites spectra, multivariate statistical analyses were performed using MetaboAnalyst (5.0), including principal component analysis (PCA) and orthogonal partial least-squares discriminant analysis (OPLS-DA). Differences among extracellular metabolites were assessed by *t*-test. The Raman shift regions with significant differences ($P \leq 0.0001$) in *t*-test were used in receiver operating characteristic curve (ROC) curves analysis to determine the performance of the classification mode.

https://doi.org/10.1021/acsomega.2c01453
ACS Omega 2022, 7, 15223−15230

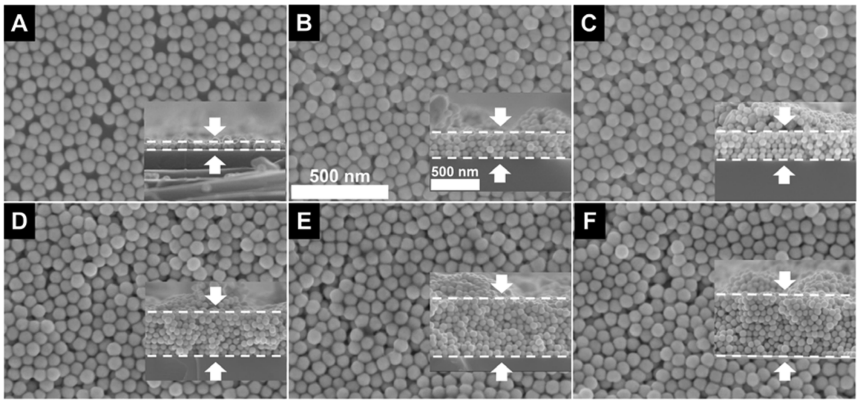

Figure 2. SEM images of Au@Ag NS 3D substrates with different layers. (A) 2, (B) 3, (C) 6, (D) 7, and (E) 9. Inset: the cross-section images of Au@Ag NS 3D substrates. The scale bar is 500 nm for both the SEM of surface and cross-section images. (F) Relationship between the thickness of Au@Ag NS 3D substrates and the NL.

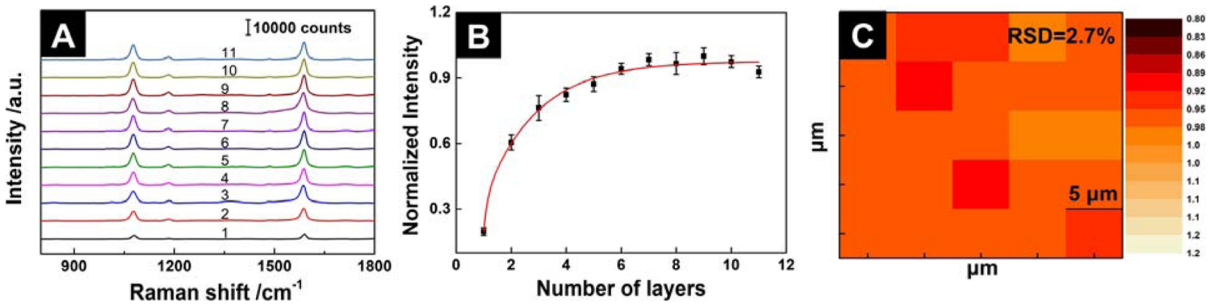

Figure 3. (A) SERS spectra of the Au@Ag NS 3D substrate with NL from 1 to 11. (B) Normalized SERS intensities of Au@Ag NS 3D substrates with NL from 1 to 11. SERS intensities at 1080 cm^{-1} of MBA were used to compare the performance. (C) Mapping image of SERS intensities on the surface of the six-layer Au@Ag NS 3D substrate. The mapping area is 25 × 25 μm^2, and the step size is 5 μm. The acquisition time of each spectrum is 1 s.

3. RESULTS AND DISCUSSION

3.1. Synthesis and Characterization of Nanoparticles. The overall experimental procedure including synthesis of nanoparticles, assembly of Au@Ag NS substrate, detection of extracellular metabolites, and statistical analysis of SERS spectra are shown in Scheme 1. A three-step procedure was adopted to fabricate the Au@Ag NS, that is, 27.6 ± 1.0 nm Au NS, 56.3 ± 2.4 nm Au NS, and 58.7 ± 2.7 nm Au@Ag NS in sequence as indicated by the TEM images (Figure 1A–D). The final Au@Ag NSs (Figure 1C) exhibit good uniformity and monodispersity. From the UV–vis–NIR spectra, it can be observed that the surface plasmon resonance of the AuNSs is red-shifted from 521 to 529 nm as the diameter increased from 27.6 ± 1.0 to 56.3 ± 2.4 nm (Figure 1E). In order to optimize the silver shell thickness, the influence of silver shell thickness was studied (Figure S1A–L). With the increment of the amount of $AgNO_3$ added into the reaction solution, the thickness of the silver shell gradually became thicker. In the meantime, the spherical structures changed when the silver shell thickness exceeded 3 nm, and a growing number of hybrid particles generated because of the self-nucleation of excess silver ions. Therefore, the uniform Au@Ag NSs with a 3 nm silver shell were selected for further use. In addition, compared to monolayer AuNSs, monolayer Au@Ag substrate exhibits much stronger SERS intensity, when using 4-MBA as a probe (Figure S2).

3.2. Characterization of Au@Ag NS Substrates. A gas–liquid interface-mediated self-assembly method was used to construct the large-area and uniform Au@Ag NS substrates from 1 to 11 layers. The characteristics of surface and cross-section morphologies are shown in Figures 2A–E and S3A–F, respectively. The Au@Ag NS substrates of different layers manifest the compact arrangement and the hierarchical structures revealing uniform SERS enhancement (Table S1, RSD ≤10%). The thickness of substrate increases uniformly with the number of layers (NL), with a good linear relationship indicating excellent uniformity of Au@Ag NS substrates (Figure 2F). Based on the fitted equation, the average thickness of each layer is 52.4 nm, which is slightly smaller than the diameter of Au@Ag NSs from TEM image. This is because there are overlaps between two layers as a result of the assembly of spheres. Due to the uniform spherical contact and the gaps between spheres, the assembled Au@Ag NS substrates can generate massive uniform hot spots between and within layers as will be discussed in the following section.

3.3. Optimization of the Au@Ag NS Substrate. For the purpose of acquiring the Au@Ag NS substrate with optimum thickness, the SERS performance of the Au@Ag NS 2D (monolayer) and 3D (multilayer) SERS substrates were evaluated using a 633 nm laser with 4-MBA as the probe. As shown in Figure 3A–B, the SERS intensity of substrates from 1 to 6 layers increases sharply with the accumulation of layers, while the SERS intensity of substrates from 6 to 11 layers remains a plateau due to limited penetration depth of the 633 nm laser.[25] Therefore, the six-layer Au@Ag NS substrate was selected as the optimal substrate.

In addition, we carried out the theoretical calculations of the electromagnetic field distribution of six-layer 3D Au@Ag

https://doi.org/10.1021/acsomega.2c01453
ACS Omega 2022, 7, 15223–15230

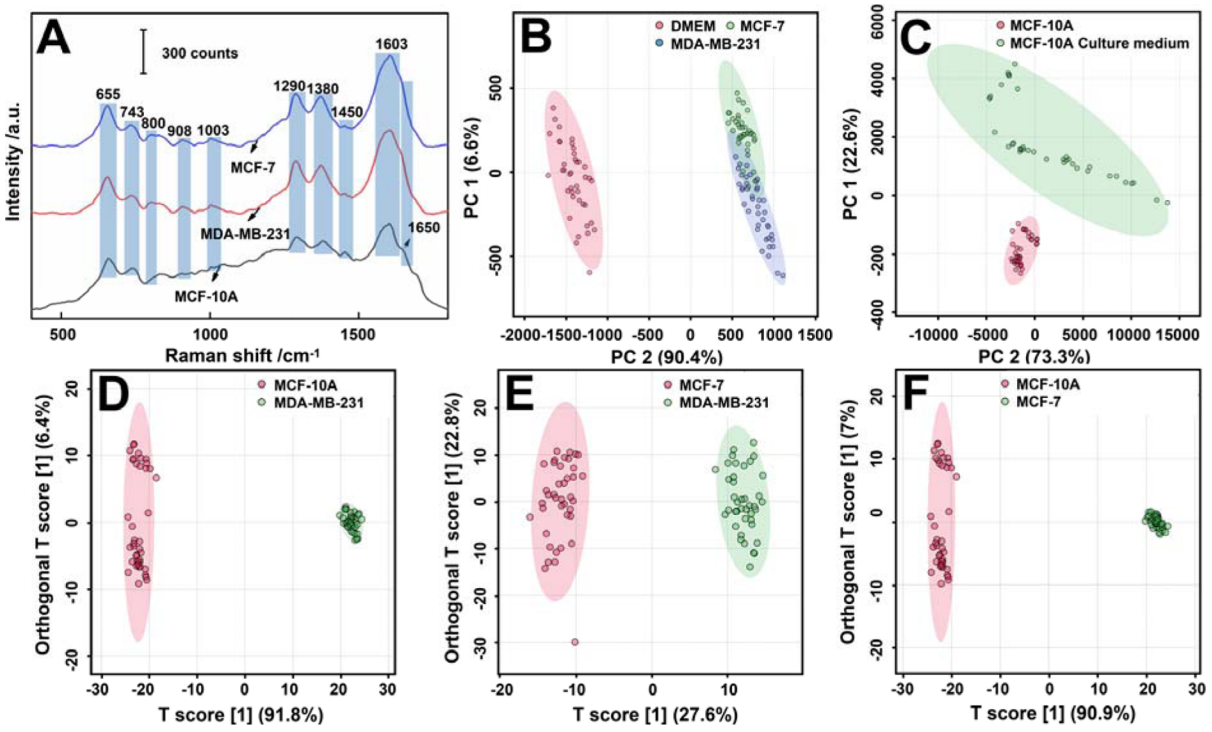

Figure 4. (A) Average SERS spectra of MDA-MB-231, MCF-7, and MCF-10A extracellular metabolites. (B) PCA plot of DMEM, MCF-7, and MDA-MB-231 extracellular metabolites. (C) PCA plot of MCF-10A culture medium and MCF-10A extracellular metabolites. (D) OPLS-DA plot of MCF-10A and MDA-MB-231 extracellular metabolites. (E) OPLS-DA plot of MCF-7 and MDA-MB-231 extracellular metabolites. (F) OPLS-DA plot of MCF-10A and MCF-7 extracellular metabolites. Each average SERS spectrum in (A) is from 40 sets of spectra and each set of spectra contains 25 individuals. Each point in (B,C) represents an average SERS spectrum of 25 individuals.

nanosphere on the Si substrate (Figure S4A−C) using the 633 nm laser illuminating from the top. Both the inter- and intralayer gaps present the hot spots, where both their intensities attenuate with the rising layer number. It should be noted that because the polarization of light is parallel to the surface, the intensity of the intralayer hot spot is stronger than that of interlayer ones. Nevertheless, for a practical optical path, it deviates from such a perfect scheme. Thus, both the inter- and intralayer hot spots play the role and contribute to the overall SERS signal intensity.

The EF of the optimal Au@Ag NS 3D substrate is calculated as 1.42×10^5 (Table S1 and Figure S5A), which is much stronger than the 3D Au nanooctahedra (AuNO) substrate reported by our group.[26] In addition, compared with the 3D AgNR substrate (RSD = 7%)[25] and 3D AuNO substrate (RSD = 6%)[26] reported from our group, the intensity RSD of the optimal Au@Ag NS 3D substrate is smaller than 3%, which proves that the optimal Au@Ag NS 3D substrates can generate more uniform hot spots (Figure 3C and Table S1). Moreover, the SERS intensity measured for 3 consecutive weeks shows no significant difference, indicating the stability in ambient conditions (Figure S5B). In short, the six-layer Au@Ag NS substrate was determined to be optimal and utilized for the following analysis.

In order to obtain the detection sensitivity of the optimal Au@Ag NS 3D substrate for biomolecules, melamine was selected for quantitative analysis, with the concentrations of 10^{-2} M to 10^{-7} M (Figure S6A,B). The 686 cm^{-1} peak in SERS spectra of melamine corresponds to the cyclic breathing pattern of melamine (Figure S6A). The LOD of melamine using optimal Au@Ag NS 3D substrate is 82 nM, which is lower than the LOD 118 nM of high-performance liquid chromatography,[31] indicating the optimal Au@Ag NS 3D substrate has quantitative detection ability for biomolecules.

3.4. SERS Analysis of Extracellular Metabolites. A normal breast cell (MCF-10A) and breast cancer cells (MCF-7 and MDA-MB-231) were cultured for experimental detection. Each cell culture medium came from an independent culture environment. In total, four culture media were collected for each strain. The metabolites contained in each sample were secreted by a plate of cells that completely covered the dish. From average SERS spectra of the three extracellular metabolites emerge obvious Raman peaks at 655, 743, 1290, 1380, 1450, and 1603 cm^{-1} (Figure 4A). Compared with MCF-10A, the average SERS spectra of MCF-7 and MDA-MB-231 extracellular metabolites have unique Raman shift regions at 800, 908, and 1003 cm^{-1}, while the average SERS spectrum of MCF-10A extracellular metabolites has a special peak at 1650 cm^{-1}. Toward these Raman shifts, the band at 655 cm^{-1} is attributed to the C−S stretching mode of cysteine.[26,32] The peak at 743 cm^{-1} is assigned to the ring vibration of thymine,[33] which is related to exosome secretion.[34] The peak at 800 cm^{-1} is attributed to tyrosine.[35] According to the report, the peak at 908 cm^{-1} is related to valine and proline.[32] The Raman shift of 1003 cm^{-1} has been designated as the aromatic ring breathing vibration of phenylalanine.[33,36] 1265−1300 cm^{-1} vibration is attributed to the amide bond.[35] The Raman shift of 1380 cm^{-1} belongs to proline, valine, or adenine.[36] The Raman shift of 1450 cm^{-1} is attributed to lipid.[38] The band at 1603 cm^{-1} is derived from C═C in-plane bending mode in tyrosine and phenylalanine.[37] The band at 1650 cm^{-1} belongs to C═C stretch of lipid.[37] According to previous reports, there are significant differences in the content of lipids and proteins between normal breast tissue and breast cancer tissue.[37] On

https://doi.org/10.1021/acsomega.2c01453
ACS Omega 2022, 7, 15223−15230

the basis of our results, average SERS spectra of breast cancer cells extracellular metabolites show significantly higher SERS intensities than normal breast cells extracellular metabolites at 800, 908, 1003, 1290, 1380, and 1603 cm^{-1}, which belong to amino acids or amide and lower SERS intensities at 1450 and 1650 cm^{-1} classified as lipids (Figure 4A). This is because breast cancer cells demand various amino acids to produce proteins for uncontrolled cell proliferation, cell division, and migration.[39] In addition, the lipid reduction in breast cancer cells extracellular secretion is due to lipid peroxidation which is a characteristic of cancer cells.[40] Based on the specified Raman shift of average SERS spectra, normal breast cells and breast cancer cells can be distinguished visually.

The average SERS spectra of two culture media (DMEM and MCF-10A culture medium) and three cell strains extracellular metabolites (MCF-10A, MCF-7, and MDA-MB-231) in Figure S7A,B show distinct characteristics. In order to assess metabolic differences between each other, PCA was performed. Multidimensional data space can be converted into a low-dimensional model plane by PCA which expresses majority of the variance within dataset using a smaller number of factors.[13] The average SERS spectra of DMEM and breast cancer cells (MCF-7 and MDA-MB-231) extracellular metabolites can be obviously distinguished by PCA (Figure 4B). Meanwhile, clear clusters of average SERS spectra of MCF-10A culture medium and MCF-10A extracellular metabolites are also revealed in PCA plot (Figure 4C). These results evidently elucidate there are different metabolites in the media of cultured cells compared with the media of uncultured cells.

When determining differences in SERS spectra of extracellular metabolites from three cell strains (MCF-10A, MCF-7, and MDA-MB-231), OPLS-DA was implemented for comparative analysis. OPLS-DA filters out the data variations in the independent variable X that are irrelevant to the categorical variable Y. Thus, the categorical information is mainly concentrated in a principal component, which makes the model more explanatory.[13] Figure 4D−F shows PC score plots without overlapped scatters among three kinds of cells (MCF-10A, MCF-7, and MDA-MB-231) extracellular metabolites. In the three models, the correlation coefficients Q^2 representing the predictive ability of the models are up to 0.997, 0.997, and 0.942, respectively ($P < 0.01$), which indicates excellent predictive capabilities of models (Figure S8A−C). Moreover, the correlation coefficients R^2Y, which represent the interpretation rate of the X and Y matrices, are 0.997, 0.998, and 0.985, respectively ($P < 0.01$), implying that models can explain data perfectly. OPLS-DA results show that different extracellular metabolites secreted by different cell strains could be detected by SERS using Au@Ag NS 3D substrates. Furthermore, with the aid of OPLS-DA, different breast cancer cells can be discriminated quickly and sensitively, indicating that this technique has the potential to screen markers from serum metabolites in a nondestructive manner for the diagnosis of breast cancer. The bands at 655, 743, 800, 908, 1003, 1290, 1380, 1450, 1603, and 1650 cm^{-1} were employed as comparison standards to obtain the most notable diversities discriminating MCF-10A, MCF-7, and MDA-MB-231 extracellular metabolites by t-test. Afterward, Raman shifts with significant differences in the t-test ($P \leq 0.0001$) are applied in ROC analysis to evaluate classification performance. The t-test analysis in Figures S9−S11 further confirmed wide discrepancies existing in extracellular metabolites of normal breast cell and breast cancer cells. From the average SERS spectra of MDA-MB-231 and MCF-7 extracellular metabolites, no obvious difference is shown (Figure 4A), but t-test demonstrated significant difference at 655, 743, 800, 1380, 1603, and 1650 cm^{-1} (Figure S11). All the regions with the optimum distinguished features confirmed in t-test correspond to the functional group of metabolites. Therefore, extracellular metabolic differences are the basis of classification. Obviously, based on this method, quick and sensitive diagnosis of breast cancer using serum by nondestructive and less harmful sample collection can be implemented. The area under the curve (AUC) of the ROC curves shown in Figure S12 at 655, 743, 800, 908, 1003, 1290, 1380, 1450, 1603, and 1650 cm^{-1}, that shown in Figure S13 at 655, 743, 800, 908, 1003, 1290, 1380, 1450, and 1650 cm^{-1}, and that shown in Figure S14 at 655, 743, 800, 1380, 1603, and 1650 cm^{-1} (Figures S12−S14) are identified over 0.75, validating the excellent performance of this classification method.

4. CONCLUSIONS

In summary, we have successfully synthesized Au@Ag NSs with excellent monodispersity, uniformity, and stability. In order to obtain the Au@Ag NS substrate with the optimum thickness, 2D and 3D Au@Ag NS SERS substrates were fabricated on the silicon wafer from 1 to 11 layers through a special self-assembly method. The unique stacking mode of 3D Au@Ag NSs provided multiple plasmonic hot spots according to the theoretical calculations of the electromagnetic field distribution. The low relative standard deviation (RSD = 2.7%) and high enhancement factor (EF = 1.42×10^5) proved the uniformity and high sensitivity. For the detection of cells extracellular metabolites (MCF-10A, MCF-7, and MDA-MB-231), distinct peaks in average SERS spectra were demonstrated. With the aid of multivariate analysis (OPLS-DA), visual aggregations were shown suggesting differences in metabolic fingerprints, and high correlation coefficients were obtained indicating the suitability of the models. The results of t-test further confirm the significant differences of the metabolite in three cell strains and demonstrate that the developed SERS analysis method is able to classify not only normal breast cells and breast cancer cells, but also different breast cancer cells. Furthermore, SERS spectra based on the Au@Ag NS 3D substrate has potential application value in diagnosis of breast cancer in a nondestructive manner.

■ ASSOCIATED CONTENT

Supporting Information

The Supporting Information is available free of charge at https://pubs.acs.org/doi/10.1021/acsomega.2c01453.

TEM images of Au@Ag NP grown in $AgNO_3$ solutions of different concentrations, SEM images of Au@Ag NS substrates with NL 1, 4, 5, 8, 10, and 11, the theoretical calculations of the electromagnetic field distribution of inter- and intralayer gaps of a six-layer Au@Ag substrate, relationship between the average enhancement factor and the NL and stability of the substrate, average SERS spectra, OPLS-DA analysis, t-test analysis, ROC analysis, tables of RSD, and EF and band assignments (PDF)

https://doi.org/10.1021/acsomega.2c01453
ACS Omega 2022, 7, 15223−15230

AUTHOR INFORMATION

Corresponding Authors

Hai-Sheng Su − *CAS Key Laboratory of Design and Assembly of Functional Nanostructures, and Fujian Provincial Key Laboratory of Nanomaterials, Fujian Institute of Research on the Structure of Matter, Chinese Academy of Sciences, Fuzhou 350002, P. R. China; Xiamen Institute of Rare Earth Materials, Haixi Institute, Xiamen Key Laboratory of Rare Earth Photoelectric Functional Materials, Chinese Academy of Sciences, Xiamen 361021, P. R. China*; Email: haishengsu@pku.edu.cn

Yun Zhang − *CAS Key Laboratory of Design and Assembly of Functional Nanostructures, and Fujian Provincial Key Laboratory of Nanomaterials, Fujian Institute of Research on the Structure of Matter, Chinese Academy of Sciences, Fuzhou 350002, P. R. China; Xiamen Institute of Rare Earth Materials, Haixi Institute, Xiamen Key Laboratory of Rare Earth Photoelectric Functional Materials, Chinese Academy of Sciences, Xiamen 361021, P. R. China; University of Chinese Academy of Sciences, Beijing 100049, P. R. China; Ganjiang Innovation Academy, Chinese Academy of Sciences, Ganzhou, Jiangxi 341000, P. R. China*; orcid.org/0000-0001-6288-4671; Email: zhangy@fjirsm.ac.cn

Authors

Zhengxia Yang − *CAS Key Laboratory of Design and Assembly of Functional Nanostructures, and Fujian Provincial Key Laboratory of Nanomaterials, Fujian Institute of Research on the Structure of Matter, Chinese Academy of Sciences, Fuzhou 350002, P. R. China; Xiamen Institute of Rare Earth Materials, Haixi Institute, Xiamen Key Laboratory of Rare Earth Photoelectric Functional Materials, Chinese Academy of Sciences, Xiamen 361021, P. R. China*

En-Ming You − *State Key Laboratory of Physical Chemistry of Solid Surfaces, College of Chemistry and Chemical Engineering, Xiamen University, Xiamen 361005, China*; orcid.org/0000-0001-6310-5908

Siying Liu − *CAS Key Laboratory of Design and Assembly of Functional Nanostructures, and Fujian Provincial Key Laboratory of Nanomaterials, Fujian Institute of Research on the Structure of Matter, Chinese Academy of Sciences, Fuzhou 350002, P. R. China; Xiamen Institute of Rare Earth Materials, Haixi Institute, Xiamen Key Laboratory of Rare Earth Photoelectric Functional Materials, Chinese Academy of Sciences, Xiamen 361021, P. R. China; University of Chinese Academy of Sciences, Beijing 100049, P. R. China*

Zihang Li − *Wenzhou-Kean University, Wenzhou, Zhejiang Province 325060, China*

Complete contact information is available at: https://pubs.acs.org/10.1021/acsomega.2c01453

Author Contributions

This manuscript was discussed and written through the contributions of all authors.

Notes

The authors declare no competing financial interest.

ACKNOWLEDGMENTS

This research was funded by the National Natural Science Foundation of China (22172131, 21503231, and 62105333) and the Xiamen Science and Technology Plan Project (3502Z20191015).

REFERENCES

(1) Loibl, S.; Poortmans, P.; Morrow, M.; Denkert, C.; Curigliano, G. Breast cancer. *Lancet* **2021**, *397*, 1750−1769.

(2) Ferlay, J.; Soerjomataram, I.; Dikshit, R.; Eser, S.; Mathers, C.; Rebelo, M.; Parkin, D. M.; Forman, D.; Bray, F. Cancer incidence and mortality worldwide: sources, methods and major patterns in GLOBOCAN 2012. *Int. J. Cancer* **2015**, *136*, E359−E386.

(3) Bhushan, A.; Gonsalves, A.; Menon, J. U. Current State of Breast Cancer Diagnosis, Treatment, and Theranostics. *Pharmaceutics* **2021**, *13*, 723−746.

(4) Kilgour, E.; Rothwell, D. G.; Brady, G.; Dive, C. Liquid Biopsy-Based Biomarkers of Treatment Response and Resistance. *Cancer Cell* **2020**, *37*, 485−495.

(5) Alba-Bernal, A.; Lavado-Valenzuela, R.; Domínguez-Recio, M. E.; Jiménez-Rodriguez, B.; Queipo-Ortuño, M. I.; Alba, E.; Comino-Méndez, I. Challenges and achievements of liquid biopsy technologies employed in early breast cancer. *EBioMedicine* **2020**, *62*, 103100−103109.

(6) Halvaei, S.; Daryani, S.; Eslami-S, Z.; Samadi, T.; Jafarbeik-Iravani, N.; Bakhshayesh, T. O.; Majidzadeh-A, K.; Esmaeili, R. Exosomes in Cancer Liquid Biopsy: A Focus on Breast Cancer. *Mol. Ther.–Nucleic Acids* **2018**, *10*, 131−141.

(7) Seah, D. S.; Leone, J. P.; Openshaw, T. H.; Scott, S. M.; Tayob, N.; Hu, J.; Lederman, R. I.; Frank, E. S.; Sohl, J. J.; Stadler, Z. K.; Erick, T. K.; Silverman, S. G.; Peppercorn, J. M.; Winer, E. P.; Come, S. E.; Lin, N. U. Perceptions of patients with early stage breast cancer toward research biopsies. *Cancer* **2021**, *127*, 1208−1219.

(8) Mann, R. M.; Cho, N.; Moy, L. Breast MRI: State of the Art. *Radiology* **2019**, *292*, 520−536.

(9) Sumkin, J. H.; Berg, W. A.; Carter, G. J.; Bandos, A. I.; Chough, D. M.; Ganott, M. A.; Hakim, C. M.; Kelly, A. E.; Zuley, M. L.; Houshmand, G.; Anello, M. I.; Gur, D. Diagnostic Performance of MRI, Molecular Breast Imaging, and Contrast-enhanced Mammography in Women with Newly Diagnosed Breast Cancer. *Radiology* **2019**, *293*, 531−540.

(10) Houssami, N.; Ciatto, S.; Macaskill, P.; Lord, S. J.; Warren, R. M.; Dixon, J. M.; Irwig, L. Accuracy and surgical impact of magnetic resonance imaging in breast cancer staging: systematic review and meta-analysis in detection of multifocal and multicentric cancer. *J. Clin. Oncol.* **2008**, *26*, 3248−3258.

(11) Morrow, M.; Waters, J.; Morris, E. MRI for breast cancer screening, diagnosis, and treatment. *Lancet* **2011**, *378*, 1804−1811.

(12) Wernli, K. J.; Ichikawa, L.; Kerlikowske, K.; Buist, D. S. M.; Brandzel, S. D.; Bush, M.; Johnson, D.; Henderson, L. M.; Nekhlyudov, L.; Onega, T.; Sprague, B. L.; Lee, J. M.; Lehman, C. D.; Miglioretti, D. L. Surveillance Breast MRI and Mammography: Comparison in Women with a Personal History of Breast Cancer. *Radiology* **2019**, *292*, 311−318.

(13) Smolinska, A.; Blanchet, L.; Buydens, L. M. C.; Wijmenga, S. S. NMR and pattern recognition methods in metabolomics: from data acquisition to biomarker discovery: a review. *Anal. Chim. Acta* **2012**, *750*, 82−97.

(14) McCartney, A.; Vignoli, A.; Biganzoli, L.; Love, R.; Tenori, L.; Luchinat, C.; Di Leo, A. Metabolomics in breast cancer: A decade in review. *Cancer Treat. Rev.* **2018**, *67*, 88−96.

(15) Zong, C.; Xu, M.; Xu, L.-J.; Wei, T.; Ma, X.; Zheng, X.-S.; Hu, R.; Ren, B. Surface-Enhanced Raman Spectroscopy for Bioanalysis: Reliability and Challenges. *Chem. Rev.* **2018**, *118*, 4946−4980.

(16) Wu, S.-R.; Tian, X.-D.; Liu, S.-Y.; Zhang, Y.; Li, J.-F. Surface-enhanced Raman spectroscopy solution and solid substrates with built-in calibration for quantitative applications. *J. Raman Spectrosc.* **2018**, *49*, 659−667.

(17) Bantz, K. C.; Meyer, A. F.; Wittenberg, N. J.; Im, H.; Kurtuluş, Ö.; Lee, S. H.; Lindquist, N. C.; Oh, S.-H.; Haynes, C. L. Recent progress in SERS biosensing. *Phys. Chem. Chem. Phys.* **2011**, *13*, 11551−11567.

(18) Huang, Z.; Zhang, A.; Zhang, Q.; Cui, D. Nanomaterial-based SERS sensing technology for biomedical application. *J. Mater. Chem. B* **2019**, *7*, 3755−3774.

(19) Liu, Y.; Wu, S.-H.; Du, X.-Y.; Sun, J.-J. Plasmonic Ag nanocube enhanced SERS biosensor for sensitive detection of oral cancer DNA based on nicking endonuclease signal amplification and heated electrode. *Sens. Actuators, B* **2021**, *338*, 129854−129862.
(20) Lin, D.; Wu, Q.; Qiu, S.; Chen, G.; Feng, S.; Chen, R.; Zeng, H. Label-free liquid biopsy based on blood circulating DNA detection using SERS-based nanotechnology for nasopharyngeal cancer screening. *Nanomedicine* **2019**, *22*, 102100.
(21) Phyo, J. B.; Woo, A.; Yu, H. J.; Lim, K.; Cho, B. H.; Jung, H. S.; Lee, M.-Y. Label-Free SERS Analysis of Urine Using a 3D-Stacked AgNW-Glass Fiber Filter Sensor for the Diagnosis of Pancreatic Cancer and Prostate Cancer. *Anal. Chem.* **2021**, *93*, 3778−3785.
(22) Gao, R.; Cheng, Z.; deMello, A. J.; Choo, J. Wash-free magnetic immunoassay of the PSA cancer marker using SERS and droplet microfluidics. *Lab Chip* **2016**, *16*, 1022−1029.
(23) Guo, J.; Zeng, F.; Guo, J.; Ma, X. Preparation and application of microfluidic SERS substrate: Challenges and future perspectives. *J. Mater. Sci. Technol.* **2020**, *37*, 96−103.
(24) Sun, H.; Cong, S.; Zheng, Z.; Wang, Z.; Chen, Z.; Zhao, Z. Metal−Organic Frameworks as Surface Enhanced Raman Scattering Substrates with High Tailorability. *J. Am. Chem. Soc.* **2018**, *141*, 870−878.
(25) Liu, S.-Y.; Tian, X.-D.; Zhang, Y.; Li, J.-F. Quantitative Surface-Enhanced Raman Spectroscopy through the Interface-Assisted Self-Assembly of Three-Dimensional Silver Nanorod Substrates. *Anal. Chem.* **2018**, *90*, 7275−7282.
(26) Han, Y.; Wu, S.-R.; Tian, X. D.; Zhang, Y. Optimizing the SERS Performance of 3D Substrates through Tunable 3D Plasmonic Coupling toward Label-Free Liver Cancer Cell Classification. *ACS Appl. Mater. Interfaces* **2020**, *12*, 28965−28974.
(27) Li, X.; Tian, X.; Liu, S.; Wu, C.; Han, Y.; Meng, L.; Song, L.; Zhang, Y. Self-assembled vertically aligned silver nanorod arrays prepared by evaporation-induced method as high-performance SERS substrates. *J. Mater. Sci.* **2020**, *55*, 14019−14030.
(28) Zhou, C.; Sun, L.; Zhang, F.; Gu, C.; Zeng, S.; Jiang, T.; Shen, X.; Ang, D. S.; Zhou, J. Electrical Tuning of the SERS Enhancement by Precise Defect Density Control. *ACS Appl. Mater. Interfaces* **2019**, *11*, 34091−34099.
(29) Fan, M.; Lai, F.-J.; Chou, H.-L.; Lu, W.-T.; Hwang, B.-J.; Brolo, A. G. Surface-enhanced Raman scattering (SERS) from Au:Ag bimetallic nanoparticles: the effect of the molecular probe. *Chem. Sci.* **2013**, *4*, 509−515.
(30) Ruan, Q.; Shao, L.; Shu, Y.; Wang, J.; Wu, H. Growth of Monodisperse Gold Nanospheres with Diameters from 20 nm to 220 nm and Their Core/Satellite Nanostructures. *Adv. Opt. Mater.* **2014**, *2*, 65−73.
(31) Qi, Y.; Li, G.; Wei, C.; Zhao, L.; Gong, B. Preparation of Magnetic Molecularly Imprinted Polymer for Melamine and its application in milk sample analysis by HPLC. *J. Biomed. Sci.* **2016**, *05*, 16−25.
(32) Yan, B.; Reinhard, B. M. Identification of Tumor Cells through Spectroscopic Profiling of the Cellular Surface Chemistry. *J. Phys. Chem. Lett.* **2010**, *1*, 1595−1598.
(33) Xiao, R.; Zhang, X.; Rong, Z.; Xiu, B.; Yang, X.; Wang, C.; Hao, W.; Zhang, Q.; Liu, Z.; Duan, C.; Zhao, K.; Guo, X.; Fan, Y.; Zhao, Y.; Johnson, H.; Huang, Y.; Feng, X.; Xu, X.; Zhang, H.; Wang, S. Non-invasive detection of hepatocellular carcinoma serum metabolic profile through surface-enhanced Raman spectroscopy. *Nanomedicine* **2016**, *12*, 2475−2484.
(34) Takahashi, A.; Okada, R.; Nagao, K.; Kawamata, Y.; Hanyu, A.; Yoshimoto, S.; Takasugi, M.; Watanabe, S.; Kanemaki, M. T.; Obuse, C.; Hara, E. Exosomes maintain cellular homeostasis by excreting harmful DNA from cells. *Nat. Commun.* **2017**, *8*, 15287−152100.
(35) Panikkanvalappil, S. R.; Hira, S. M.; Mahmoud, M. A.; El-Sayed, M. A. Unraveling the biomolecular snapshots of mitosis in healthy and cancer cells using plasmonically-enhanced Raman spectroscopy. *J. Am. Chem. Soc.* **2014**, *136*, 15961−15968.
(36) Moreira, L. P.; Silveira, L., Jr.; da Silva, A. G.; Fernandes, A. B.; Pacheco, M. T. T.; Rocco, D. D. F. M. Raman spectroscopy applied to identify metabolites in urine of physically active subjects. *J. Photochem. Photobiol., B* **2017**, *176*, 92−99.
(37) Lazaro-Pacheco, D.; Shaaban, A. M.; Rehman, S.; Rehman, I. Raman spectroscopy of breast cancer. *Appl. Spectrosc. Rev.* **2019**, *55*, 439−475.
(38) Shao, L.; Zhang, A.; Rong, Z.; Wang, C.; Jia, X.; Zhang, K.; Xiao, R.; Wang, S. Fast and non-invasive serum detection technology based on surface-enhanced Raman spectroscopy and multivariate statistical analysis for liver disease. *Nanomedicine* **2018**, *14*, 451−459.
(39) Abramczyk, H.; Brozek-Pluska, B. Raman imaging in biochemical and biomedical applications. Diagnosis and treatment of breast cancer. *Chem. Rev.* **2013**, *113*, 5766−5781.
(40) Brożek-Płuska, B.; Placek, I.; Kurczewski, K.; Morawiec, Z.; Tazbir, M.; Abramczyk, H. Breast cancer diagnostics by Raman spectroscopy. *J. Mol. Liq.* **2008**, *141*, 145−148.

https://doi.org/10.1021/acsomega.2c01453
ACS Omega 2022, 7, 15223−15230